Nigerian Journal of Technology (NIJOTECH)
Vol. 43, No. 3, September, 2024, pp.526 - 533
www.nijotech.com

Print ISSN: 0331-8443
Electronic ISSN: 2467-8821
https://doi.org/10.4314/njt.v43i3.15

THERMAL PROFILING OF A SWITCHED RELUCTANCE MACHINE WITH 6/4 POLE TOPOLOGY

AUTHORS:
C. E. Abunike[1,*], J. U. Jeff-Matthew[2], C. C. Awah[3], O. I. Okoro[4], B. I. Oruh[5], and A. J. Onah[6]

AFFILIATIONS:
[1,2,3,4,6]Department of Electrical/Electronic Engineering, Michael Okpara University of Agriculture, Umudike, Nigeria
[5]Department of Mathematics, Michael Okpara University of Agriculture, Umudike, Nigeria

***CORRESPONDING AUTHOR:**
Email: abunike.emmanuel@mouau.edu.ng

ARTICLE HISTORY:
Received: 10 March, 2024.
Revised: 23 July, 2024.
Accepted: 07 August, 2024.
Published: 20 September, 2024.

KEYWORDS:
Cooling jacket, Finite element analysis, Switched reluctance motor, Temperature constraints, Thermal analysis.

ARTICLE INCLUDES:
Peer review

DATA AVAILABILITY:
On request from author(s)

EDITORS:
Ozoemena Anthony Ani

FUNDING:
TETFUND Institutional based research grant

Abstract
This paper presents a thermal analysis of a switched reluctance machine (SRM) with a 6/4 pole topology. Employing a two-dimensional thermal finite element model in Maxwell 2D integrated into a lumped parameter thermal network in MotorCAD, the research aims to realize critical temperature points within the SRM, focusing on the windings and laminations to identify potential hotspots. To ensure continuous operation without compromising structural integrity, temperature constraints of 150 °C for the windings and 100 °C for the laminations were enforced. The investigation extends to the cooling domain by utilizing a housing cooling jacket and ethylene glycol and water ratio (EGW) of 60/40 as the cooling fluid. An exploration of various volume flow rates revealed that 15 l/min was the optimal choice, resulting in the lowest temperatures observed in both the winding and lamination regions. This study emphasizes the shift of hotspot temperatures from the stator winding in the low-speed region to the rotor in the high-speed range, impacting the overall continuous operating time. This holistic examination significantly contributes to a broader understanding of electric machine thermal management and offers invaluable insights for practical applications in electric vehicles, manufacturing processes, and various industrial settings.

1.0 INTRODUCTION
The evolution of electric machines and their practical applications in various industries necessitate a comprehensive understanding of their thermal behavior for optimal performance and reliability [1]. In the last decade, the significance of thermal analysis of electrical machines has increased substantially, paralleled by the increasing popularity of specialized software dedicated to this crucial function [2-4]. This trend underscores the growing awareness of the role of temperature considerations in optimizing the performance, safety, and longevity of electric machines.

The surge in electric vehicle development and the advent of high-power motors have heightened the importance of thermal analysis for understanding the impact of heat generation during power transmission on motor performance and safety [5]. The temperature rise within electric machines, if left unchecked, can surpass the limits of insulation materials, resulting in insulation failure or accelerated aging effects, thereby adversely affecting the life expectancy of the machine [4], [6-7]. In pursuit of enhanced overall economics, it

HOW TO CITE:
Abunike, C. E., Jeff-Matthew, J. U., Awah, C. C., Okoro, O. I., Oruh, B. I., and Onah, A. J. "Thermal Profiling of a Switched Reluctance Machine with 6/4 Pole Topology", *Nigerian Journal of Technology*, 2024; 43(3), pp. 526 – 533; *https://doi.org/10.4314/njt.v43i3.15*

has become evident that highly loaded electric motors are often constrained by their operating temperature. Consequently, a balance between heating and cooling is a decisive factor in the design and operation of these motors. For a homologous series of motors, the progression of the temperature rise becomes a fundamental element influencing the output, size, weight, and cost [8].

Switched reluctance machines (SRMs) have garnered attention because of their simplicity, high reliability, and cost-effectiveness [9]. Precise examination of the thermal field within the SRM is essential to ensure its longevity and safety [10]. Driven by the reluctance torque resulting from changes in the resistance of the magnetic circuit, the SRMs have coils solely on the stator, presenting a structurally simpler alternative to induction and synchronous motors [11]. The ability of the SRM to withstand high-speed rotations and high-temperature operations, while exhibiting resilience to impacts and vibrations, has led to its increasing application in devices such as washing machines [12], vacuum cleaners [13], electric bicycles [14], electric [15-16] or hybrid vehicles [17] in response to environmental concerns and energy challenges.

Given the diverse and demanding operational scenarios encountered by SRMs, the development of a comprehensive thermal map is imperative for the effective design of thermal management systems. This study is based on an in-depth investigation into the thermal characteristics and profiling of a SRM with 6/4 pole topology, with the aim of contributing valuable insights to the broader field of electric machine thermal management. Through a two-dimensional thermal finite element model and detailed simulations, this study explored the intricate interdependencies between motor design, cooling strategies, and performance. This investigation ultimately provides an understanding of the thermal behavior of SRMs under diverse operational conditions.

The remaining sections of this paper are structured as follows: Section 2 outlines the methodology, focusing on finite element analysis (FEA) and thermal analysis of the SRM. This is followed by Section 3, which delves into the results and discussion, offering a comprehensive analysis of the findings. Finally, Section 4 concludes the paper, summarizing key insights and implications drawn from the study.

2.0 METHODOLOGY

2.1 Finite Element Analysis of Switched Reluctance Motor

The two-dimensional FEA approach is used in the SRM model to solve the voltage equations as well as the magnetic field in the air gap, windings, and iron core. The magnetic field in the SRM is governed by Maxwell's equation [18]:

$$\nabla \times H = J \quad (1)$$

$$\nabla \times E = -\frac{\partial B}{\partial t} \quad (2)$$

Where, H is the magnetic field strength, ∇ is the del operator, E is electric field strength, J is current density, and B is magnetic flux density. Owing to the low frequencies employed in electrical machines, it is believed that the polarization and displacement currents are insignificant. As these elements are not encompassed within Equation (2), the analysis is denoted as quasi-static. The material equation can be derived by incorporating the reluctivity, v:

$$H = vB \quad (3)$$

While the magnetic flux density is defined by the magnetic vector potential A in the following manner:

$$B = \nabla \times A \quad (4)$$

By substituting equations (3) and (4) into equation (1), the core expression for the formulation of vector potential of the magnetic field is:

$$\nabla \times (v\nabla \times A) = J \quad (5)$$

As illustrated in Equations (6) and (7), the foundation of the 2D model relies on the assumption that both the current density and magnetic vector potential have components solely along the z-axis, with their values determined on the xy plane.

$$A = A(x, y)e_z \quad (6)$$

$$J = J(x, y)e_z \quad (7)$$

Here, e_z indicates a vector unit aligned with the direction of the z-axis. Consequently, equation (5) transforms into:

$$-\nabla \cdot (v\nabla A) = J \quad (8)$$

The current density is defined as:

$$J = \sigma E \quad (9)$$

Here, the conductivity is represented by σ. Solving (5) and (9) yields:

$$\nabla \times E = -\frac{\partial}{\partial t}\nabla \times A \quad (10)$$

This condition is fulfilled by defining the current density as:

$$J = -\sigma \frac{\partial A_s}{\partial t} - \sigma \nabla \emptyset \quad (11)$$

Where $\emptyset$ and A_s represent the electric potential and electric scalar potential, respectively.

The motion of the rotor over successive time intervals is governed by solving the equations describing its dynamics, except the assumption that speed is constant [19].

$$J\frac{d\omega_m}{dt} = T_e - T_L \quad (12)$$

$$\omega_m = \frac{d\theta_m}{dt} \quad (13)$$

Here, J, T_e, ω_m, θ_m, and T_L correspond to the moment of inertia, electromagnetic torque, angular speed, angular position of the rotor, and load torque, respectively. At the commencement of each time increment, the rotor's updated position is defined, and a distinct mesh is created within the air gap. The efficiency of the machine with respect to speed is given as:

$$\eta(s) = \frac{T(s)\times\omega(s)}{V(s)\times I(s)} \times 100\% \quad (14)$$

Where *T(s)* is the torque as a function of speed, *ω(s)* is the angular speed (in rad/s), which can be related to the motor speed in RPM, *V(s)* is the input voltage as a function of speed, and *I(s)* is the input current as a function of speed.

The electromagnetic torque is determined through the application of the virtual work principle.

$$T_e = \frac{\partial}{\partial\theta_m}\int_\Omega \left(\int_0^H B \cdot dH\right) d\Omega \quad (15)$$

Where T_e, B, H, Θ_m, and Ω represent the electromagnetic torque, magnetic flux density, magnetic field, rotor position, and the domain, respectively. The integration area was exclusively focused on the air gap. The approach used in [20] was implemented for the finite element analysis, in which the virtual motion was governed by a mapping function while the air-gap mesh is unchanged. The studied machine is a 3-phase 1.5 kW switched reluctance motor with 6/4 pole topology and is star-connected. Figure 1 shows the meshing and magnetic flux lines of the motor and its specifications are listed in Table 1.

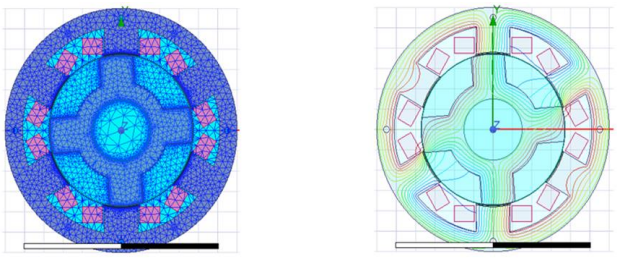

Figure 1: (a) Mesh map in Maxwell 2D (b) Flux lines plot

Table 1: Specifications of the studied motor

Parameter	Value
Power output	1.5 kW
Rated voltage	380 V
Rated speed	1500 rpm
Pole number of stator/rotor	6/4
Outer diameter of the stator	120 mm
Inner diameter of the stator	75 mm
Inner diameter of the rotor	30mm
Pole embrace of stator	0.45
Pole embrace of rotor	0.3
Thickness of the stator yoke	12 mm
Thickness of the rotor yoke	9 mm

2.2 Thermal Study of the Motor

The approach outlined in this section is utilized to assess the comprehensive performance of the motor across the speed range. The finite element model was exported to the MotorCAD environment in the <.mot> format using the Maxwell interface. Nevertheless, an extra constraint was imposed on the temperature of the SRM, ensuring continuous operation without the risk of overheating. A thermal study of the motor was conducted using MotorCAD and a lumped parameter thermal network. The cooling of the motor involved the utilization of a cooling jacket within the housing, with EGW 60/40 chosen as the cooling medium. Figure 2 shows the 3D model of the motor with the cooling jacket.

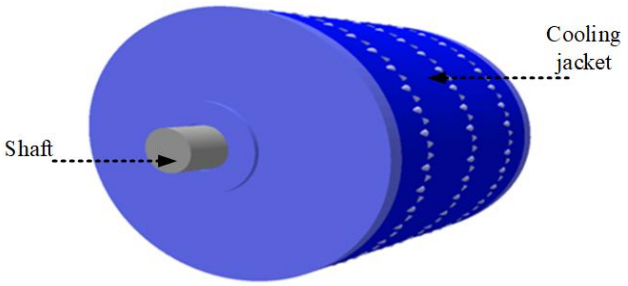

Figure 2: 3D Model of the motor with stator cooling

The process illustrated in Figure 3 is implemented in the determination of the SRM temperature by combining all the components of the heat path into a single thermal circuit system.

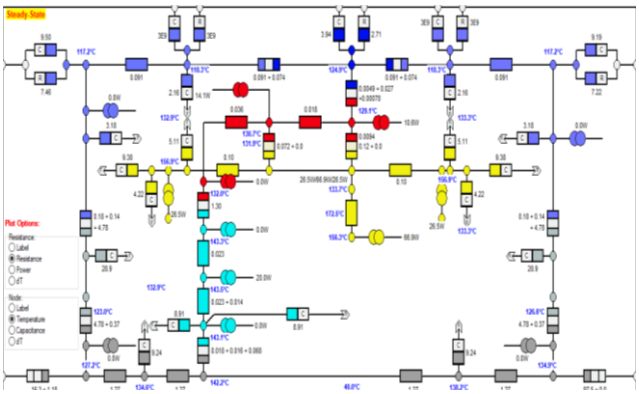

Figure 3: Steady state thermal network of the model in MotorCAD

The housing and stator lamination interface gap measures 0.01 mm. The chosen fluid had a thermal conductivity of 0.3692 W/m/^{0}C and a density of 1065 kg/m^3, whereas the slot liner employed in the investigation had a thermal conductivity of 0.21 W/m/^{0}C. To maintain a constant inlet temperature of

45 °C, three volume flow rates (5, 15, and 25 l/min) were examined to determine the temperature limit of the SRM. The selected flow rate, which ensured an acceptable temperature limit, was used for the motor final examination. Based on the results of this study, temperature constraints of 150 °C for the windings and 100 °C for the laminations were established, as similarly conducted in [21].

Accurately calculating motor losses during operation is crucial for determining the temperature field. The entire loss function is computed as follows:

$$P = P_{cu} + P_{Fe} + P_s \quad (16)$$

Where the total and additional loss are represented as P and P_s, copper and iron loss as P_{cu} and P_{Fe}. In steady-state motor operation, copper loss is [19, 22]:

$$P_{cu} = mI_{rms}^2 R_{phase} \quad (17)$$

Here, phase number and resistance are m and R_{phase} while I_{rms} is the effective winding current.

Typically, determining additional loss is challenging without a precise formula. In practical calculations, it is estimated to be approximately 6% of the total loss, as described in [23]:

$$P_s = (P_1 - P_2) \times 6 \quad (18)$$

Here, the output and input powers are P_2 and P_1. The iron loss is expressed as:

$$P_{Fe} = P_h + P_c + P_e \quad (19)$$

Where P_e, P_c, and P_h denote the excess loss, eddy-current loss, and hysteresis loss, respectively.

$$P_h = \sum_{i=1}^{n} k_h \cdot f \cdot \left[B_{tm}^2 \cdot \left(1 + c \cdot \frac{1}{B_{tm}} \sum_{i=1}^{N} \Delta B_{ti}\right) + B_{rm}^2 \cdot \left(1 + c \cdot \frac{1}{B_{rm}} \sum_{i=1}^{N} \Delta B_{ri}\right)\right] \quad (20)$$

$$P_c = \sum_{i=1}^{n} k_c \cdot (if)^2 \cdot \left(B_{ri}^2 + B_{ti}^2\right) \quad (21)$$

$$P_e = \sum_{i=1}^{n} k_e \cdot (if)^{1.5} \cdot \left(B_{ri}^{1.5} + B_{ti}^{1.5}\right) \quad (22)$$

Here, k_h, k_c, and k_e represent coefficients for hysteresis, eddy-current, and excess losses, respectively. f is the fundamental frequency, i is the harmonic order, and c is a constant (usually it is 0.65). B_{ti} and B_{ri} denote the amplitude of tangential and radial magnetic flux density at the i^{th} time, while B_{tm} and B_{rm} represent their respective maximum values [25]. Table 2 shows the thermal properties of the motor materials.

Table 2: Thermal properties of electrical materials

Materials	Conductivity (W/m/K)	Density (kg/m^3)	Heat capacity (J/kg/K)
Aluminum	168	2790	833
Copper	401	8933	385
M19 24G	28	7800	460
Air	0.0242	1.225	1006.43

3.0 RESULTS AND DISCUSSION

In this section, the obtained simulated results are discussed. For continuous operation, it becomes necessary to measure the motor temperature. This is crucial for assessing the efficiency of the motor, as illustrated in Figure 4, which depicts the efficiency plot across the entire operating range.

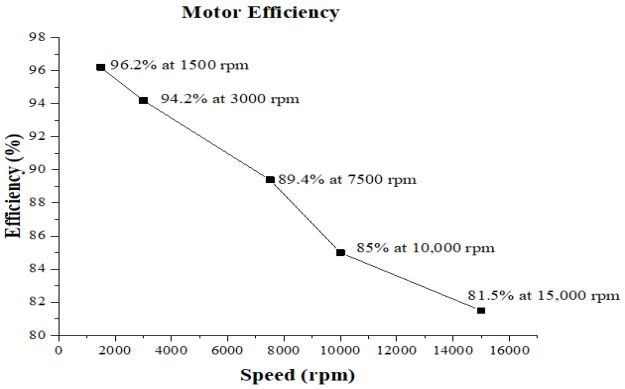

Figure 4: Efficiency variation at various operating speeds of the motor

Figure 4 shows that when the motor speed increases, the efficiency of the motor decreases because of the increased rotor core loss in the high-speed region. Hence, the best performance of the motor is achievable in the low-speed region, with an efficiency of 95.2% at 1500 rpm. The efficiency plot provides insights into how the motor performs under different speed conditions, aiding in optimizing its usage and ensuring sustained effectiveness.

The respective charts of the winding and lamination temperatures are shown in Figures 5 (a) and 5 (b), respectively. The plots show the examination of three volume flow rates aimed at observing the temperature increase in the motor within low-speed (1,500 rpm) and high-speed (15,000 rpm) regions.

The flow rates I, II, and III were 5, 15, and 25 l/min, respectively. Figure 5 indicates that flow rate II (15 l/min) yielded the lowest temperatures at both low-speed (251.5°C in winding and 150.2°C in lamination) and high-speed (158.3°C in winding and 198.1°C in lamination) regions. Therefore, it was chosen for further thermal analysis over a broad speed range. The dynamics of the winding, rotor surface, stator surface, and housing temperatures over time at the four speeds are presented in Figures 6, 8, 10, and 12. In these figures, "A" and "B" denote the winding and lamination temperature limits, respectively, while "C" indicates the maximum continuous operating time.

Figures 6 and 7 reveal that, in the low-speed range, the determining factor for sustaining continuous operation lies in the temperature limitation imposed on the winding. Specifically, Figure 6 (b) highlights that, at

this speed, the stator winding is the hotspot for temperature.

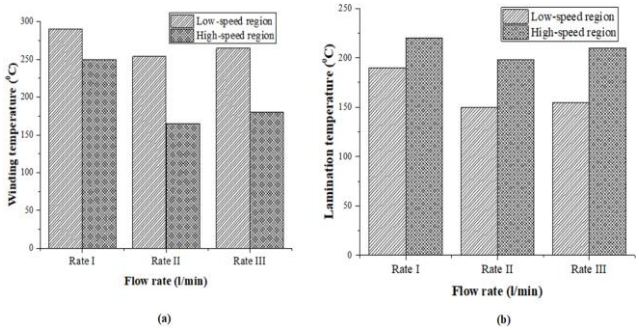

Figure 5: Temperature at different operating speeds (a) Winding temperature (b) Lamination temperature

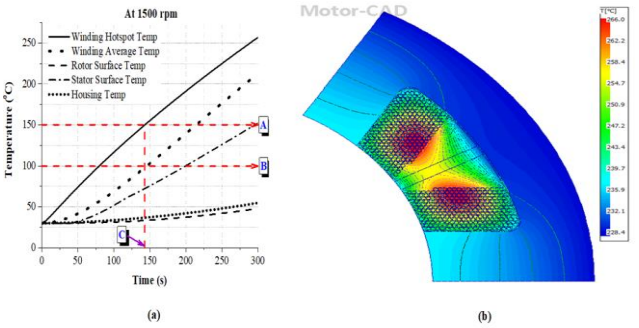

Figure 6: Thermal behavior at 1500 rpm (a) Temperature with time (b) Steady-state temperature of cross-section of the stator

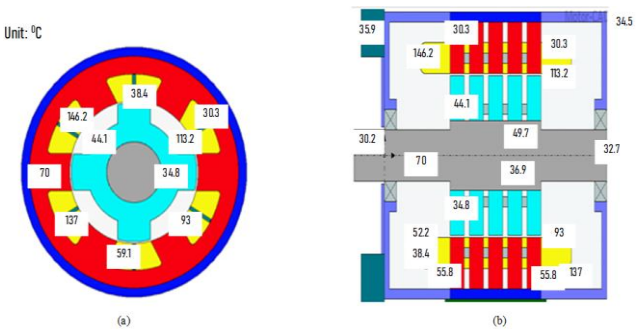

Figure 7: Temperature distribution for continuous operation at speed of 1500 rpm at 143.6 s: (a) Radial cross section, and (b) Axial cross section

The radial and axial temperatures of the rotor's cross-section at 1500 rpm are illustrated in Figure 7. At this speed, the winding hotspot reaches the 150°C constraint at 143.6 seconds, as depicted in Figure 6 (a). A similar trend is observed at 3000 rpm, as illustrated in Figure 8. At 3000 rpm, Figure 8 indicates a maximum continuous operating time of 163 seconds. The radial and axial temperatures of the rotor cross-section at this speed are presented in Figure 9. Notably, the maximum continuous operating time increases with the rise in speed within the low-speed range.

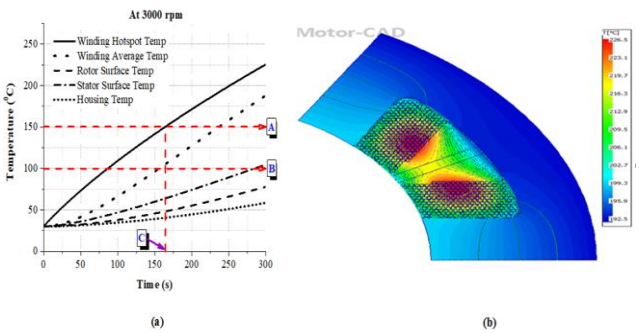

Figure 8: Thermal behavior at 3000 rpm (a) Temperature with time (b) Steady-state temperature of cross-section of the stator

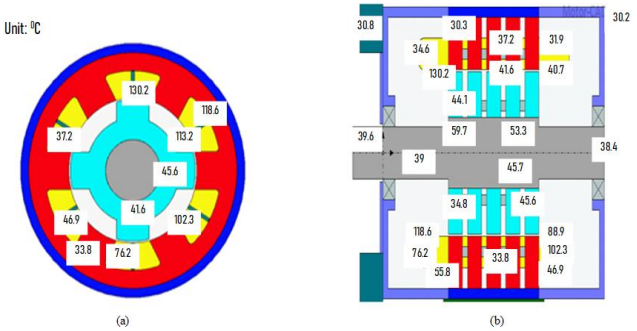

Figure 9: Temperature distribution for continuous operation at speed of 3000 rpm at 163 s: (a) Radial cross section, and (b) Axial cross section

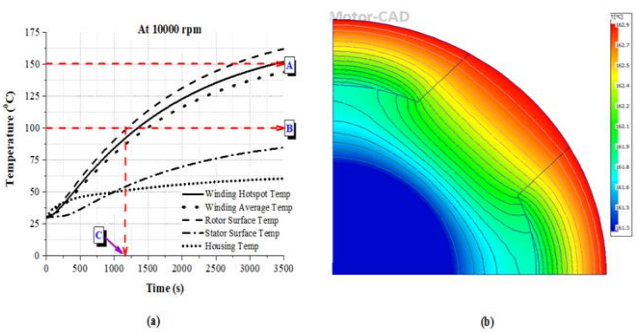

Figure 10: Thermal behavior at 10,000 rpm (a) Temperature with time (b) Steady-state temperature of cross-section of the rotor

Figure 10 illustrates the steady-state temperature distribution of the stator when the motor operates at 3000 rpm, highlighting the hotspot temperature on the stator winding in the low-speed region. At 10,000 rpm, the continuous operating time extends to 1205 seconds, as demonstrated in Figure 10. The steady-state temperature distributions of the rotor when the motor is operating at 10000 rpm and 10,000 rpm are shown in Figure 10 (b).

Figure 11 displays the radial and axial temperatures of the rotor cross-section at 10,000 rpm. Similar trends are evident for the motor operating at 15,000 rpm, illustrated in Figure 12, where the continuous operating time is recorded at 755 seconds. This suggests that as the motor speed rises in the high-speed region, the overall continuous time decreases. The steady-state temperature distributions of the rotor at 15,000 rpm are presented in Figure 12 (b).

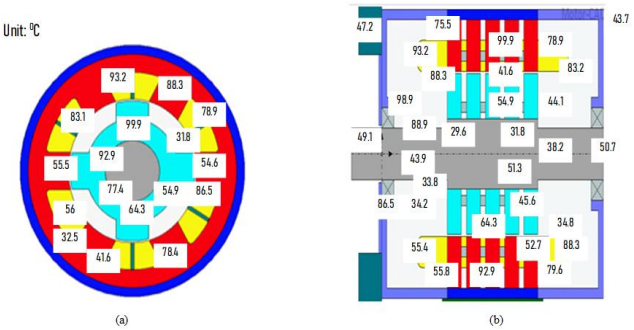

Figure 11: Temperature distribution for continuous operation at speed of 10,000 rpm at 1205s: (a) Radial cross section, and (b) Axial cross section

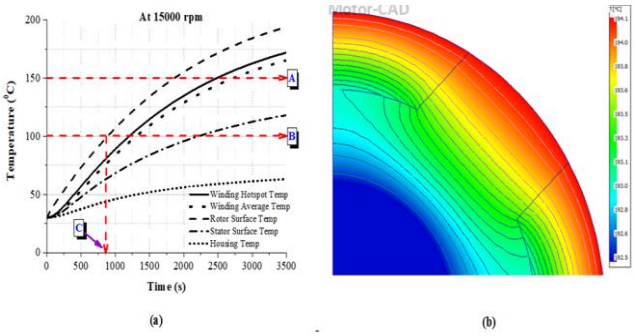

Figure 12: Thermal behavior at 15,000 rpm (a) Temperature with time (b) Steady-state temperature of cross-section of the stator

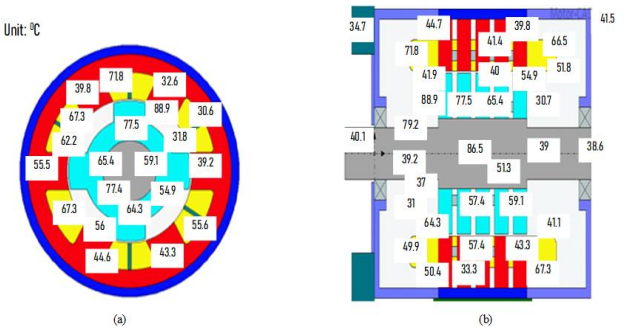

Figure 13: Temperature distribution for continuous operation at speed of 15,000 rpm at 775 s: (a) Radial cross section, and (b) Axial cross section

Figure 13 illustrates the radial and axial temperatures of the rotor cross-section at a speed of 15,000 rpm. The steady-state temperature distributions of the rotor when the motor operates at 15,000 rpm are presented in Figure 12 (b). These depictions reveal that the hotspot temperature is situated on the rotor in the high-speed region.

The temperature analyses in Figures 6, 8, 10, and 12 offer crucial insights into SRM's continuous operation under varying speeds. Notably, the hotspot temperatures observed play a significant role in determining maximum continuous operating time, which shifts from stator winding in the low-speed region to the rotor in the high-speed range. This information is vital for managing temperatures in practical SRM applications, ensuring the motor performance, reliability, and suitability across diverse industrial settings, including electric vehicles and manufacturing processes.

4.0 CONCLUSION

In this study, we analyzed the temperature fields in a Switched Reluctance Motor (SRM) using ANSYS Maxwell and MotorCAD, focusing on the effects of speed on temperature distribution and efficiency. The key findings are summarized as follows:

1. The motor efficiency declines with increasing speed, primarily owing to the heightened rotor core loss in the high-speed region. The optimal motor performance, with an efficiency of 95.2%, was achieved in the low-speed region at 1500 rpm,
2. The study identified 15 l/min as the optimal cooling rate that minimized the temperature levels in the winding and lamination regions. This rate was chosen for an additional thermal analysis across a wide speed range, underscoring the practical importance of an effective cooling strategy,
3. The continuous operation of the motor is constrained by the winding temperature in the low-speed region, whereas the rotor surface hotspot acts as a limiting factor in the high-speed region. These insights are crucial for establishing operational boundaries and ensuring the longevity of SRM,
4. The continuous overall time decreased with increasing motor speed in the high-speed region, and exhibited an opposite trend in the low-speed region. These findings provide valuable guidance for understanding the temporal dynamics of SRM operations, and
5. This study presents the radial and axial temperature distributions of the rotor cross section at five operating speeds, offering a comprehensive visual representation of the SRM's thermal behavior across diverse operational scenarios.

This study enhances the understanding of SRM thermal behavior and informs future research and design for efficient electric machines.

REFERENCES

[1] Ghahfarokhi, P. S., Podgornovs, A., Kallaste, A., Cardoso, A. J. M., Belahcen, A., Vaimann, T., Tiismus, H. and Asad, B. "Opportunities and challenges of utilizing additive manufacturing approaches in thermal management of electrical machines", *IEEE Access*, 9, pp. 36368-36381, 2021.

[2] Bramerdorfer, G., Lei, G., Cavagnino, A., Zhang, Y., Sykulski, J. and Lowther, D. A. "More robust and reliable optimized energy conversion facilitated through electric machines, power electronics and drives, and their control: State-of-the-art and trends", *IEEE Transactions on Energy Conversion*, vol. 35, no. 4, pp.1997-2012, 2020.

[3] Yaabari, N., Okoro, O. I., and Akpama, E. J. ''Matlab-based simulations of a three-phase induction motor for dynamic studies'', *Nigerian Journal of Technology*, vol .41, no. 6, pp. 1000-1007, 2022.

[4] Gundabattini, E., Mystkowski, A., Idzkowski, A. and Solomon, D. G. "Thermal mapping of a high-speed electric motor used for traction applications and analysis of various cooling methods—A review", *Energies*, vol. 14, no. 5, p.1472, 2021.

[5] Chidambaram, K., Ashok, B., Vignesh, R., Deepak, C., Ramesh, R., Narendhra, T. M., Muhammad Usman, K. and Kavitha, C. "Critical analysis on the implementation barriers and consumer perception toward future electric mobility", *Proceedings of the Institution of Mechanical Engineers, Part D: Journal of Automobile Engineering*, vol. 237, no. 4, pp. 622-654, 2023.

[6] Sayed, E., Abdalmagid, M., Pietrini, G., Sa'adeh, N.M., Callegaro, A.D., Goldstein, C. and Emadi, A. "Review of electric machines in more-/hybrid-/turbo-electric aircraft", *IEEE Transactions on Transportation Electrification*, vol 7, no. 4, pp. 2976-3005, 2021.

[7] Mastoi, M. S., Zhuang, S., Munir, H. M., Haris, M., Hassan, M., Alqarni, M. and Alamri, B. "A study of charging-dispatch strategies and vehicle-to-grid technologies for electric vehicles in distribution networks", *Energy Reports*, vol. 9, pp.1777-1806, 2023.

[8] Boglietti, A., Cavagnino, A., Staton, D., Shanel, M., Mueller, M. and Mejuto, C. "Evolution and modern approaches for thermal analysis of electrical machines", *IEEE Transactions on industrial electronics*, vol. 56, no. 3, pp. 871-882, 2009.

[9] Bostanci, E., Moallem, M., Parsapour, A. and Fahimi, B. "Opportunities and challenges of switched reluctance motor drives for electric propulsion: A comparative study", *IEEE transactions on transportation electrification*, vol. 3, no. 1, pp. 58-75, 2017.

[10] Elhomdy, E., Liu, Z. and Li, G. "Thermal and mechanical analysis of a 72/48 switched reluctance motor for low-speed direct-drive mining applications", *Applied Sciences*, vol. 9, no. 13, p. 2722, 2019.

[11] Jack, A. G., Mecrow, B. C. and Haylock, J. A. "A comparative study of permanent magnet and switched reluctance motors for high-performance fault-tolerant applications", *IEEE transactions on industry applications*, vol. 32, no. 4, pp. 889-895, 1996.

[12] Asgar, M., Afjei, E., Behbahani, A. and Siadatan, A. "A 12/8 double-stator switched reluctance motor for washing machine application", *6th Power Electronics, Drive Systems & Technologies Conference*, pp. 168-172, 2015.

[13] Ma, P., Ding, W. and Du, C. "Design and Performance Analysis of a Super High-Speed Switched Reluctance Motor for Vacuum Cleaners", *25th International Conference on Electrical Machines and Systems*, pp. 1-5, 2015.

[14] Lin, J., Schofield, N. and Emadi, A. "External-rotor 6/10 switched reluctance motor for an electric bicycle", *IEEE Transactions on Transportation electrification*, vol. 1, no. 4, pp. 348-356, 2015.

[15] Gan, C., Wu, J., Sun, Q., Kong, W., Li, H. and Hu, Y. "A review on machine topologies and control techniques for low-noise switched reluctance motors in electric vehicle applications", *IEEE Access*, 6, pp. 31430-31443, 2018.

[16] Abunike, E. C., Okoro, O. I. and Davidson, I. E. "Design Considerations and Performance Prediction of an External Rotor 6/10 Switched Reluctance Motor for Electric Vehicle Applications", *IEEE PES/IAS PowerAfrica*, pp. 1-5, 2021.

[17] Takeno, M., Chiba, A., Hoshi, N., Ogasawara, S., Takemoto, M. and Rahman, M.A. "Test results and torque improvement of the 50-kW switched reluctance motor designed for hybrid electric vehicles", *IEEE Transactions on*

Industry Applications, vol. 48, no. 4, pp.1327-1334, 2012.

[18] Aljaism, W. A. "Switched reluctance motor: Design, simulation and control", Doctoral dissertation, University of Western Sydney, Australia, 2007.

[19] Abunike, E. C., Okoro, O. I. and Davidson, I. E. "Thermal Analysis of an Optimized Switched Reluctance Motor for Enhanced Performance", *IEEE PES/IAS PowerAfrica*, pp. 1-5, 2021.

[20] Cervera, M., Codina, R. and Galindo, M. "On the computational efficiency and implementation of block-iterative algorithms for nonlinear coupled problems", *Engineering computations*, vol. 13, no. 6, pp. 4-30, 1996.

[21] Burress, T. A., Campbell, S. L., Coomer, C., Ayers, C. W., Wereszczak, A. A., Cunningham, J. P., Marlino, L. D., Seiber, L. E. and Lin, H. T. "Evaluation of the 2010 Toyota Prius hybrid synergy drive system", Oak Ridge National Laboratory, Oak Ridge, TN (United States). Power Electronics and Electric Machinery Research Facility, 2011.

[22] Babayomi, O., and Balogun, A. ''Internal Model Loss Minimization Control of Permanent Magnet Synchronous Machine'', *Nigerian Journal of Technology*, vol. 40, no. 1, pp. 97-108, 2021.

[23] Materu, P. N. and Krishnan, R. "Estimation of switched reluctance motor losses", *IEEE Transactions on Industry Applications*, vol. 28, no. 3, pp. 668-679, 1992.

[24] Memon, A. A., Bukhari, S. S. H. and Ro, J. S. "Experimental determination of equivalent iron loss resistance for prediction of iron losses in a SRM", *IEEE Transactions on Magnetics*, vol. 58, no. 2, pp.1-4, 2021.

[25] Yan, W., Chen, H., Liu, X., Ma, X., Lv, Z., Wang, X., Palka, R., Chen, L. and Wang, K. "Design and multi-objective optimisation of SRM with iron loss", *IET Electric Power Applications*, vol. 13, no. 4, pp. 435-444, 2019.